Scientific Reports

https://doi.org/10.1038/s41598-026-49676-9

Article in Press

An edge-cloud collaborative fault diagnosis method for high-resistivity faults in low-voltage distribution networks considering metering uncertainties

Received: 9 January 2026

Accepted: 16 April 2026

Published online: 27 April 2026

Cite this article as: Cheng B., Sun S., Li S. *et al.* An edge-cloud collaborative fault diagnosis method for high-resistivity faults in low-voltage distribution networks considering metering uncertainties. *Sci Rep* (2026). https://doi.org/10.1038/s41598-026-49676-9

Baohua Cheng, Shuxian Sun, Siwei Li, Yimeng Zhang, Yun Li & Yiying Zhang

An edge-cloud collaborative fault diagnosis method for high-resistivity faults in low-voltage distribution networks considering metering uncertainties

Baohua Cheng[1], Shuxian Sun[1], Siwei Li[2], Yimeng Zhang[3], Yun Li[4], and Yiying Zhang[5,*]

[1]State Grid Tianjin Marketing Service Center, Tianjin, 300000, China
[2]Beijing Fibrlink Communications Co., Ltd., Beijing, 100000, China
[3]Tianjin Institute of Metrological Supervision and Testing, Tianjin, 300000, China
[4]Shenzhen Clou Intelligence Industry Co.,Ltd., Shenzhen, 518000, China
[5]College of Artificial Intelligence, Tianjin University of Science and Technology, Tianjin, 300457, China
[*]yiyingzhang@tust.edu.cn

ABSTRACT

To address the issue of weak characteristics and susceptibility to environmental noise and measurement errors in high-impedance faults (HIFs) in low-voltage distribution networks, this paper proposed an edge-cloud collaborative fault diagnosis method (ECCFD) that considers the metering uncertainty of smart meters. First, to address the common problems in low-cost smart meters such as transformer errors, clock asynchrony, and quantization noise, a statistical modeling method for measurement uncertainty is established. This uncertainty is encoded into multi-dimensional node features through time window partitioning and feature statistics, improving the robustness of feature representation. Second, an edge-cloud collaborative diagnostic architecture for low-voltage distribution networks is constructed. At the edge, high-order harmonic ratios, order components, and statistical features are extracted and normalized to reduce communication load and mitigate the impact of load fluctuations on feature stability. Then, a graph model is constructed in the cloud based on the distribution network topology. A Bayesian graph convolutional neural network (BGCN) is introduced to perform joint inference on node states. Variational inference and Monte Carlo sampling are used to estimate fault probability and prediction uncertainty. Finally, simulation and comparative experiments verified that the constructed method can still maintain high diagnostic accuracy and stability under conditions of high noise and significant measurement uncertainty, providing technical support for robust and reliable diagnosis of high-resistance faults in the actual operation of smart grids.

Abbreviations

HIFs	High-impedance Faults
ECCFD	Edge-cloud Collaborative Fault Diagnosis
BGCN	Bayesian Graph Convolutional Neural Network
GNN	Graph Neural Networks
GCN	Graph Convolutional Network
SVM	Support Vector Machine
CNN	Convolutional Neural Network
GAT	Graph Attention Network

Introduction

With the rapid growth of distributed power sources and electricity loads, the operating environment of low-voltage distribution networks is becoming increasingly complex[1–3]. High-impedance faults (HIFs), due to their small fault current amplitude and strong randomness, are difficult to reliably detect by traditional protection devices, and have become a significant problem restricting the safe operation of distribution networks[4–6]. In recent years, the large-scale deployment of smart meters has provided a new data foundation for the perception of distribution network operating status and fault diagnosis. However, limited by cost and communication conditions, the measurement accuracy of smart meters is limited and susceptible to factors such as transformer errors, clock asynchrony, and quantization noise, which further mask the weak characteristics of HIFs[7–9]. Therefore, how to achieve robust and reliable diagnosis of high-impedance faults under measurement uncertainty remains a key problem that urgently needs to be solved in the field of smart grids.

Existing research on high-resistance faults mostly employs data-driven methods, extracting harmonic features, sequence component features, or time-domain statistical features, and combining them with models such as deep neural networks for fault identification[10–12]. These methods have achieved some success under ideal measurement conditions, but they typically assume that the measurement data is accurate and time-synchronized, ignoring unavoidable uncertainties in low-cost smart meters, such as transformer errors, clock drift, and quantization noise[13–15]. In actual operating environments, when load fluctuations intensify or communication conditions are limited, measurement errors often exhibit randomness and cumulative characteristics, further masking the already subtle characteristics of high-resistance faults[16,17]. Existing methods typically mitigate the impact of noise through simple filtering or normalization, but they do not statistically characterize the reliability of the measurement data, leaving the model lacking adaptability in the face of abnormal measurements or amplified noise. Therefore, it is necessary to explicitly introduce a description of measurement uncertainty during the feature construction stage, enabling the model to not only focus on the numerical magnitude of the features themselves but also perceive their stability and reliability, thereby improving the robustness of fault diagnosis under complex operating conditions.

With the continuous expansion of power distribution networks and the rapid growth in the number of smart meters, centralized data processing methods are gradually revealing limitations in terms of communication bandwidth, computing resources, and system scalability[18–20]. On the one hand, fault diagnosis methods that rely entirely on the cloud require frequent uploading of raw or high-frequency measurement data, which can easily lead to communication congestion and diagnostic delays, making it difficult to meet the real-time requirements of power distribution networks[21,22]. On the other hand, some studies have pushed diagnostic tasks down to the edge, using only local information for judgment[23–25]. While these methods have fast response times, they often struggle to maintain stable performance in complex network structures due to a lack of modeling of the global topology and node relationships. Furthermore, edge devices have limited computing resources, making it difficult to directly deploy complex deep learning models. Against this backdrop, constructing an edge-cloud collaborative architecture that rationally divides computing tasks is particularly important, allowing the edge to focus on data preprocessing and feature extraction, while the cloud is responsible for global information fusion and high-precision inference, thereby achieving a balance between diagnostic performance and engineering feasibility.

In recent years, graph neural networks (GNNs) have attracted widespread attention in fault diagnosis and condition assessment due to their ability to effectively characterize distribution network topology and uncover spatial correlations between nodes[26–28]. However, most existing GNN-based methods still employ deterministic parameter modeling, outputting only a single prediction result and lacking characterization of prediction uncertainty[29,30]. In high-resistance fault diagnosis scenarios, due to weak fault characteristics, significant measurement noise, and increased diversity of operating conditions, models often face the problem of inconsistent distributions between training data and actual operating data. In this situation, deterministic models are prone to overconfident judgments regarding noise or abnormal samples, increasing the risk of false alarms or missed alarms. Existing studies mostly use threshold adjustment or empirical rules for post-processing, but these methods lack a unified probabilistic interpretation. While probabilistic modeling has been successfully applied to remaining useful life prediction via sequential variational autoencoders[31], its application to smart grid fault diagnosis remains limited. Furthermore, although topology-aware strategies have shown promise in handling cross-domain shifts[32], few studies explicitly model the cognitive uncertainty induced by measurement noise in low-cost sensors. Therefore, introducing probabilistic reasoning mechanisms into GNNs to explicitly model cognitive uncertainty at the model level is of great significance for achieving reliable and interpretable high-resistance fault diagnosis.

In summary, this paper constructs an edge-cloud collaborative fault diagnosis method (ECCFD) for high-resistance fault diagnosis in smart grids. First, the measurement uncertainty of smart meters is modeled. Second, node features are constructed at the edge through sub-window statistical feature extraction. Finally, a graph model is built based on the distribution network topology, and a Bayesian graph convolutional neural network (BGCN) is introduced in the cloud for fault inference. Monte Carlo prediction is used to output the fault probability and uncertainty, achieving robust and reliable fault diagnosis. Experimental results show that this method exhibits superior diagnostic performance compared to traditional methods under various noise conditions, providing an effective solution for high-resistance fault detection in the actual operation of smart grids. The main innovations of this paper are as follows:

1. Measurement uncertainties are explicitly encoded into the characteristics of smart grid nodes through mean and variance, providing robust input for subsequent BGCN and improving sensitivity to high-resistance faults and noise immunity.

2. The edge-cloud collaborative concept is combined with the measurement uncertainty characteristics to ensure both the real-time performance and robustness of the diagnostic system in high-resistance fault diagnosis.

3. A joint output of fault probability and model uncertainty is achieved by combining BGCN with Monte Carlo prediction, providing reliable diagnostics for smart grids.

This paper is mainly organized as follows: Section 2 introduces the basic theories required for this paper; Section 3 introduces the ECCFD method considering the metering uncertainty of smart meters; Section 4 introduces the experimental verification and results; and Section 5 provides a conclusion.

Basic Theories

As one of the representative algorithms of GNNs, graph convolutional network (GCN)[33] achieves smoothing and propagation of features in the neighborhood by performing local weighted averaging of node features under the constraints of graph structure. First, a graph structure is constructed, which is typically represented as:

$$G = (\mathfrak{X}, \Im) \tag{1}$$

where $\mathfrak{X} = \{\mathfrak{X}_1, \mathfrak{X}_2, \ldots, \mathfrak{X}_N\}$ is a set of nodes with N nodes, $\Im$ is the set of edges. The adjacency matrix $A \in R^{N\times N}$ can be represented as:

$$A_{ij} = \begin{cases} 1, (\mathfrak{X}_1, \mathfrak{X}_2) \in \Im \\ 0, otherwise \end{cases} \tag{2}$$

The degree matrix $D \in R^{N\times N}$ can be represented as:

$$D_{ii} = \sum_j A_{ij} \tag{3}$$

For node i, its new feature can be defined as the average of the features of its neighbors:

$$H = D^{-1}AX \tag{4}$$

where X represents the original feature of node i. However, node i does not use its own feature x_i in the above formula, so a self-loop needs to be added. The adjacency matrix $\tilde{A}$ and the corresponding degree matrix $\tilde{D}$ after adding the self-loop are:

$$\tilde{A} = A + I \tag{5}$$

$$\tilde{D}_{ii} = \sum_j \tilde{A}_{ij} \tag{6}$$

The average of the neighbor characteristics after adding a self-loop is:

$$H = \tilde{D}^{-1}\tilde{A}X \tag{7}$$

This way, nodes retain their own information while aggregating their neighbors. The height nodes will dominate feature propagation if used $\tilde{D}^{-1}\tilde{A}$ directly, leading to numerical instability. Therefore, symmetric normalization is necessary.

$$\hat{A} = \tilde{D}^{-\frac{1}{2}}\tilde{A}\tilde{D}^{-\frac{1}{2}} \tag{8}$$

Thus, the standard formula for single-layer GCNN propagation[34] is:

$$H^{(l+1)} = \sigma(\hat{A}H^{(l)}W^{(l)}) \tag{9}$$

where $H^{(l)}$ represents the features of the l-th layer node, $W^{(l)}$ represents the trainable weight matrix, $\hat{A}$ represents the normalized adjacency matrix, and $\sigma()$ represents the non-linear activation function.

Edge-cloud collaborative fault diagnosis method considering the metering uncertainty of smart meters

Modeling the measurement uncertainty of smart meters

Given a low-voltage distribution network, where each smart meter at a node is represented as $i = 1, \ldots, N$, and each meter collects electrical quantities within a time window T, the actual electrical quantities under ideal conditions can be represented as:

$$x_i(t) = \begin{bmatrix} V_i(t) \\ I_i(t) \\ \phi_i(t) \end{bmatrix} \tag{10}$$

where $V_i(t)$ is the effective voltage value, which directly reflects the node potential level and is an important indicator of load changes and fault occurrence; $I_i(t)$ is the effective current value, which describes the energy flow and load stress in the branch; $\phi_i(t)$ is the voltage-current phase angle, which represents the phase difference between voltage and current, reflects the load characteristics and system power flow state, and will show subtle but discriminative disturbances when high-resistance faults occur.

Under theoretical analysis and ideal simulation conditions, the above three quantities can be regarded as the actual state quantities of the system. However, in actual distribution network operation, the effective values of voltage, current, and phase angle at nodes cannot be obtained directly and without error. These electrical quantities are usually measured indirectly by smart meters installed on the user side or at distribution nodes. However, due to limitations in equipment cost and deployment conditions, these measurement devices have significant constraints in terms of hardware accuracy, sampling frequency, and time synchronization capabilities. Therefore, in high-resistance fault diagnosis, measurement uncertainty modeling must be used to bridge the gap between the actual state and the available data. The measured values are expressed as:

$$\tilde{x}_i(t) = x_i(t) + \varepsilon_i(t) \tag{11}$$

where $x_i(t)$ is the true value and $\varepsilon_i(t)$ represents the overall measurement error.

1) Modeling of amplitude and phase measurement errors

The current transformers and other components of smart meters introduce unavoidable random errors. These errors are modeled as follows:

$$\varepsilon_i^{(m)}(t) \sim N(0, \Sigma_i^{(m)}) \tag{12}$$

Its covariance matrix is defined as:

$$\Sigma_i^{(m)} = \begin{bmatrix} \sigma_V^2 & 0 & 0 \\ 0 & \sigma_I^2 & 0 \\ 0 & 0 & \sigma_\phi^2 \end{bmatrix} \tag{13}$$

That is, the observed value given by the smart meter is:

$$\tilde{V}_i(t) = V_i(t) + \varepsilon_{V,i}(t), \varepsilon_{V,i}(t) \sim N(0, \sigma_V^2) \tag{14}$$

$$\tilde{I}_i(t) = I_i(t) + \varepsilon_{I,i}(t), \varepsilon_{I,i}(t) \sim N(0, \sigma_I^2) \tag{15}$$

$$\tilde{\phi}_i(t) = \phi_i(t) + \varepsilon_{\phi,i}(t), \varepsilon_{\phi,i}(t) \sim N(0, \sigma_\phi^2) \tag{16}$$

where σ_V, σ_I, and σ_ϕ represent the standard deviations of the effective voltage value measurement error, the current RMS measurement error, and the phase angle measurement error, respectively. A Gaussian distribution is used to characterize the unavoidable random error; this uncertainty belongs to the inherent noise of the data and cannot be eliminated even with infinite data.

2)Modeling time-asynchronous uncertainty

Due to the lack of precise time synchronization, the actual measurement time of the nth meter is:

$$\tilde{t}_i = t + \Delta t_i \tag{17}$$

The time offset follows a zero-mean Gaussian distribution:

$$\Delta t_i \sim N(0, \sigma_t^2) \tag{18}$$

where σ_t^2 represents the variance, and under the assumption of small time offset, the real signal can be approximated as a first-order expansion:

$$x_i(\tilde{t}_i) \approx x_i(t) + \frac{dx_i(t)}{dt}\Delta t_i \tag{19}$$

Based on the above formula, time asynchrony can be transformed into measurement uncertainty, and the introduction of difficult-to-interpret assumptions in high-order modeling can be avoided, providing an analytical expression for the propagation of uncertainty.

3) Modeling information missing and communication uncertainty

To describe missing data, a random mask variable is defined as follows:

$$m_i(t) \sim Bernoulli(p_i) \tag{20}$$

where *Bernoulli* is a binary random variable:

$$m_i(t) = \begin{cases} 1, data\ successfully\ received \\ 0, data\ missing \end{cases} \tag{21}$$

And it satisfies:

$$\begin{aligned} &\Pr(m_i(t) = 1) = p_i \\ &\Pr(m_i(t) = 0) = 1 - p_i \end{aligned} \tag{22}$$

where p_i represents the packet reception probability at node i. The final comprehensive measurement model is:

$$\tilde{x}_i(t) = m_i(t) \odot (x_i(t) + \varepsilon_i^{(m)}(t)) \tag{23}$$

By modeling uncertainties such as amplitude error, phase deviation, time asynchrony, and communication packet loss, the reliability of measurement data can be explicitly perceived and quantified, clearly defining the uncertainty boundaries of the measurement data. This allows for the characterization of the statistical relationship between actual measurement data and ideal electrical states, providing a reliable data foundation for subsequent feature construction and fault reasoning.

Edge-side multidimensional feature extraction

Smart meters typically only provide low-frequency statistics or low-order harmonic information, failing to capture the original waveforms at high sampling rates. Furthermore, the significant characteristics of HIF are not reflected in instantaneous amplitude, but rather in statistical behavior and instability. Therefore, directly using the original measurements is neither practical nor consistent with physical mechanisms. It is necessary to extract representative features while considering measurement uncertainties, ensuring that the node features input to the GCN can both characterize HIF information and reflect the reliability of the input noise.

1) Higher harmonic ratio:

$$f_{i,1} = \frac{\sum_{h=h_{\min}}^{h_{\max}} \left| I_i^{(h)}(t) \right|}{\left| I_i^{1}(t) \right|} \tag{24}$$

where $I_i^{(h)}$ is the amplitude of the h-th harmonic, $h_{\min}$ and $h_{\max}$ are the selected range of higher harmonics, and $I_i^1(t)$ is the fundamental amplitude. This feature is used to describe the nonlinear load caused by HIF.

2) Harmonic energy variance:

The energy of the h-th harmonic within window T is:

$$E_{h,i}(t) = \sum_{\tau=t-T}^{t} \left| I_{h,i}(\tau) \right|^2 \tag{25}$$

The harmonic energy variance is:

$$f_{i,2} = Var(E_{h,i}(t)) \tag{26}$$

This feature can capture the randomness of HIF.

3) Positive/negative sequence voltage ratio:

$$f_{i,3} = \frac{V_i^{(-)}}{V_i^{(+)}}, f_{i,4} = \frac{V_i^{(0)}}{V_i^{(+)}} \tag{27}$$

where $V_i^{(+)}$, $V_i^{(-)}$ and $V_i^{(0)}$ represent positive-sequence, negative-sequence, and zero-sequence voltages, respectively, which can describe the imbalance of the power grid.

4) Ordinal component variance:

$$f_{i,5} = Var(\frac{V_i^{(-)}}{V_i^{(+)}}), f_{i,6} = Var(\frac{V_i^{(0)}}{V_i^{(+)}}) \tag{28}$$

HIF disrupts three-phase balance, but its amplitude is significantly affected by operating conditions. The imbalance characteristics can be more robustly characterized by the sequence component ratio.

5) Current kurtosis[35]:

$$f_{i,7} = \frac{1}{T} \sum_{t=1}^{T} Kurtosis(I_i(t)) \tag{29}$$

$$Kurtosis(I_i) = \frac{\mathrm{E}\left[(I_i - \mu_I)^4 \right]}{\sigma_I^4} \tag{30}$$

where I represents current, μ_I represents the mean of the current, and σ_I represents the standard deviation. Arc-type HIF exhibits significant randomness and intermittency, and its statistical distribution often shows heavy-tailed characteristics; kurtosis can effectively capture this phenomenon.

6) Current deflection[35]:

$$f_{i,8} = \frac{1}{T} \sum_{t=1}^{T} Skewness(I_i(t)) \tag{31}$$

$$Skewness(I_i) = \frac{\mathrm{E}\left[(I_i - \mu_I)^3 \right]}{\sigma_I^3} \tag{32}$$

where I represents current, μ_I represents the mean of the current, and σ_I represents the standard deviation. Due to the uncertainty in input measurement, the feature itself should also be considered a random variable:

$$f_{i,k} \sim N(\mu_{i,k}, \sigma_{i,k}^2) \tag{33}$$

The mean represents the expected behavior of the feature, and the variance reflects the reliability resulting from the propagation of measurement uncertainty. Ultimately, the feature of each node is represented as a joint vector of the mean and uncertainty.

$$z_i = [\mu_{i,1}, \ldots, \mu_{i,K}, \sigma_{i,1}, \ldots, \sigma_{i,K}] \tag{34}$$

where K represents the total number of features, $\mu_{i,K}$ represents the mean of the features within the time window, and $\sigma_{i,K}$ represents the standard deviation of the features within the time window.

The main function of the edge-side multidimensional feature extraction module is to transform the noisy measurement data collected by smart meters into stable, compact, and physically interpretable node feature representations. By extracting features such as higher harmonic ratios, order components, and statistical moments at the edge, and combining this with sub-window statistics to encode measurement uncertainties, this module effectively suppresses the impact of load fluctuations and random noise while reducing communication load. The resulting features not only retain the discrimination information for high-impedance faults but also provide a reliable input foundation for probabilistic inference based on graph models in the cloud.

Cloud-based probabilistic fault diagnosis based on Bayesian graph convolutional neural networks

The multi-dimensional feature matrix obtained from the edge side is transmitted to the cloud. Based on BGCN, probabilistic inference is performed on the edge features to output fault identification results and quantify prediction uncertainty, thereby achieving high-confidence fault diagnosis and false alarm suppression. Since the voltage and current disturbances of each smart meter propagate along the topology, the graph structure of the distribution network is first constructed:

$$G_{BGCN} = (\text{ƛ}_{BGCN}, \Im_{BGCN}) \tag{35}$$

where ƛ_{BGCN} represents a smart meter node and $\Im_{BGCN}$ represents an electrical connection. The weighted adjacency matrix of this graph structure is:

$$A_{BGCN_{ij}} = \begin{cases} \exp(-Z_{ij}), (i,j) \in \Im \\ 0, otherwise \end{cases} \tag{36}$$

where Z_{ij} represents the line impedance between node i and node j. The larger the impedance, the weaker the coupling. The above weighted adjacency matrix is standardized as follows:

$$\tilde{A}_{BGCN} = D_{BGCN}^{-1/2} A_{BGCN} D_{BGCN}^{-1/2}, D_{BGCN_{ii}} = \sum_j A_{BGCN_{ij}} \tag{37}$$

where D_{BGCN} is the degree matrix. The graph structure is then propagated based on BGCN graph convolution:

$$H_{BGCN}^{(l+1)} = g(\tilde{D}_{BGCN}^{-1/2} \tilde{A}_{BGCN} \tilde{D}_{BGCN}^{-1/2} H_{BGCN}^{(l)} W_{BGCN}^{(l)}) \tag{38}$$

where H_{BGCN} is the hidden layer, $H_{BGCN}^{(1)} = g(\tilde{D}_{BGCN}^{-1/2} \tilde{A}_{BGCN} \tilde{D}_{BGCN}^{-1/2} z_i W_{BGCN}^{(l)})$ and $g()$ is the activation function. Unlike traditional GCNs, the weights $W_{BGCN}^{(l)}$ of each layer in BGCN are random variables, enabling the model to output a predicted distribution rather than a single point result, through Bayesian modeling[36]:

$$W_{BGCN}^{(l)} \sim N(\mu_W^{(l)}, \sum_W^{(l)}) \tag{39}$$

where $\mu_W^{(l)}$ is the most probable weight, and $\sum_W^{(l)}$ is the diagonal covariance. Random weights are used in the calculation during graph convolution propagation. The distribution of the optimized model parameters is obtained through variational inference, and the training loss function is as follows:

$$L = E_{q(W)}[\log p(y|X,W)] - KL(q(W||p(W))) \tag{40}$$

The first term of the loss function guarantees the model's predictive ability, while the second term, KL divergence, constrains model complexity and avoids overfitting. Then, through multiple forward propagations using Monte Carlo sampling, the model obtains a prediction distribution, where the mean represents the failure probability and the variance reflects the model's cognitive uncertainty. This uncertainty increases significantly in high-noise and information-scarce scenarios. Since the ideal formula $p(y|z) = \int p(y|z,W)p(W|D)dW$ for Bayesian prediction is not analytical, it is approximated by S sampling iterations:

$$p(y_i|z) \approx \frac{1}{S} \sum_{s=1}^{S} p(y_i|z, W^{(s)}) \tag{41}$$

where $p(y|z,W^{(s)})$ is the forward propagation output $f(z,W^{(s)})$ of the BGCN network:

$$\hat{y}_i^{(s)} = f(z_i;W^{(s)}) \tag{42}$$

After multiple samplings, multiple predictions are made based on the model.

$$\bar{y}_i = \frac{1}{S}\sum_{s=1}^{S}\hat{y}_i^{(s)} \tag{43}$$

where z_i represents the multidimensional feature $z_i = [\mu_{i,1},\ldots,\mu_{i,K},\sigma_{i,1},\ldots,\sigma_{i,K}]$ obtained from the edge side, $W^{(s)}$ represents the network weight sampled from the Bayesian parameter distribution in the s-th iteration, and $\hat{y}^{(s)}$ represents the prediction result of BGCN in the s-th iteration. Cognitive uncertainty is calculated by the following formula:

$$Var(y) = \frac{1}{S}\sum_{s=1}^{S}\left(\hat{y}_i^{(s)} - \bar{y}_i\right)^2 \tag{44}$$

During the inference phase, instead of using fixed weights, we sample S sets of weights from the posterior distribution $q_\theta(W_{BGCN})$. This is implemented by performing S stochastic forward passes for each input sample. The Monte Carlo approximation error converges at $O(1/S)$. If S is too small, the high-variance estimator fails to adequately capture the posterior distribution, making the uncertainty gating erratic. If S is too large, the latency increases linearly while the accuracy gain diminishes marginally. The final prediction and uncertainty are computed as the mean and variance of the S output probabilities, respectively. Finally, fault decisions are made based on failure probability and cognitive uncertainty.

$$\begin{cases} \bar{y}_i > \tau_p, Var(y_i) < \tau_u, fault\ alarm \\ \bar{y}_i > \tau_p, Var(y_i) \geq \tau_u, suspected\ fault, further\ observation\ required \\ \bar{y}_i \leq \tau_p, normal \end{cases} \tag{45}$$

where thresholds τ_p and τ_u which not only leverages historical data and expert experience, but also dynamically calibrates using a data-driven operational procedure on an independent validation set.

The cloud-based fault diagnosis module implements probabilistic inference of edge-side features based on BGCN. Under physical topology constraints, this module models the spatial correlation between nodes through graph convolution operations and models network weight parameters as random variables, thus explicitly characterizing the model's cognitive uncertainty. Through multiple forward propagations using Monte Carlo sampling, the model not only outputs the probability of fault occurrence for each node but also quantifies the level of uncertainty in the prediction results. In scenarios with weak high-resistance fault characteristics and significant measurement noise, this module effectively suppresses false alarms caused by uncertain measurements, providing high-confidence fault diagnosis support for power grid operation. In summary, the overall flowchart of the ECCFD method considering the metering uncertainty of smart meters is shown in Fig. 1, and the pseudocode is shown in Algorithm 1.

Algorithm1:	**End-to-End Pseudo-code of the Proposed ECCFD Method**
1	**Module I: Uncertainty Modeling and Masking Strategy**
2	**for** each meter node $i \in V$ **do**
3	Model measurement errors: $\varepsilon_{V,i}(t) \sim \mathcal{N}(0,\sigma_V^2)$, $\varepsilon_{I,i}(t) \sim \mathcal{N}(0,\sigma_I^2)$
4	Model time asynchrony: $\delta t_i \sim \mathcal{U}(-\tau_{max},\tau_{max})$
5	Model communication packet loss: $m_i(t) \sim \text{Bernoulli}(1-p_{loss})$
6	Obtain raw uncertain measurements: $\tilde{x}_i(t) = g(x_i(t),\varepsilon_i(t),\delta t_i)$
7	**if** $m_i(t) == 0$ **then**
8	Apply Missing Value Imputation: $\tilde{x}_i(t) \leftarrow 0$ (Zero-padding)
9	Append a binary indicator flag to explicitly learn the missingness.
10	**end if**
11	**end for**
12	**Module II: Edge-side Feature Extraction and Normalization**
13	**for** each node $i \in V$ **do**

Table 1 – Continued

Algorithm1:	**End-to-End Pseudo-code of the Proposed ECCFD Method**
	Divide time window T into K sub-windows
	for each sub-window $k = 1, \ldots, K$ **do**
	Extract harmonic ratios, sequence components, and statistical moments
	end for
	Aggregate sub-window features to form node feature vector: $z_i = [\mu_i, \sigma_i]$
	Feature Normalization: Apply Z-score standardization using training set statistics:
	$\hat{z}_i = (z_i - \mu_{train})/\sigma_{train}$
	end for
	Module III: Cloud-side Topology-Aware BGCN Inference
	Step 1: Physical Graph Construction
	for each electrical line edge $(i, j) \in E$ **do**
	Obtain physical line impedance: $Z_{ij} = R_{ij} + jX_{ij}$
	Assign impedance-weighted adjacency: $A_{ij} = \exp(-\lvert Z_{ij} \rvert)$
	end for
	Compute normalized symmetric adjacency matrix $\tilde{A}$.
	Step 2: Variational Training (Offline)
	for each GNN layer $l = 1, \ldots, L$ **do**
	Parameterize weight distributions: $W^{(l)} \sim \mathcal{N}(\mu_W^{(l)}, \Sigma_W^{(l)})$
	end for
	Optimize objective: $\mathcal{L} = \mathbb{E}_{q(W)}[\log p(Y\|Z,W)] - \mathrm{KL}(q(W)\|p(W))$
	Step 3: Monte Carlo Prediction (Online)
	for MC sample $s = 1, \ldots, S$ (e.g., $S = 50$) **do**
	Sample network weights using reparameterization: $W^{(s)} \sim q(W)$
	Forward propagation: $\hat{y}^{(s)} = f(\hat{Z}, \tilde{A}; W^{(s)})$
	end for
	Compute predictive mean (Probability): $\bar{y} = \frac{1}{S}\sum_s \hat{y}^{(s)}$
	Compute predictive uncertainty (Variance): $U = \frac{1}{S}\sum_s (\hat{y}^{(s)} - \bar{y})^2$
	Step 4: Three-Level Uncertainty Gating Decision
	if $\bar{y} \leq \tau_p$ **then return** "Normal"
	else if $\bar{y} > \tau_p$ **and** $U \geq \tau_u$ **then return** "Suspected Fault (Requires Observation)"
	else return "Confirmed Fault Alarm"
	end if

Experimental verification

Simulation platform data verification

To verify the effectiveness of the proposed method, this section first uses the IEEE 33-bus as a test platform to simulate data for method verification. The fault resistance range is $R_f \in [200, 2000]\,\Omega$, and line nodes are randomly selected as fault locations. Smart meters are deployed at each node, with a sampling frequency of 6.4kHz. Measurement variables include $\tilde{V}_i(t)$, $\tilde{I}_i(t)$, $\tilde{\phi}_i(t)$, and amplitude noise, phase noise, time asynchrony, and random communication packet loss are introduced to simulate the real measurement environment of low-cost smart meters. HIF events are generated by controlling the fault resistance Rf and switch timing, providing exact ground-truth labels. In the experimental verification, 60% of the data was used for training, 20% for verification, and 20% for testing. All hyperparameter tuning and early stopping were performed solely based on the validation set performance. The leakage-safe event-based data splitting protocol for simulation platform data is shown in Table 2.

To ensure reproducibility and facilitate fair comparisons, the detailed parameter settings and computational environment are specified as follows. Both simulation and field data were segmented using a sliding window of T=0.2s with 50% overlap. For each window, a 9-dimensional physics-informed feature vector was extracted at the edge. The proposed BGCN consists of two Bayesian graph convolutional layers with 64 hidden units and ReLU activation, followed by a fully connected layer for classification. The model was trained for 200 epochs using the Adam optimizer with a learning rate of 0.005, weight decay of $5e^{-4}$, and a batch size of 64. To ensure robust evaluation, all experiments were repeated with 5 distinct random seeds (42, 123, 2021, 2022, 2023). The edge-side feature extraction is lightweight, taking <5ms per window on a standard ARM Cortex-M4 MCU (simulated), while the cloud-side inference latency is about 12ms per batch on an NVIDIA GeForce RTX 3060 GPU,

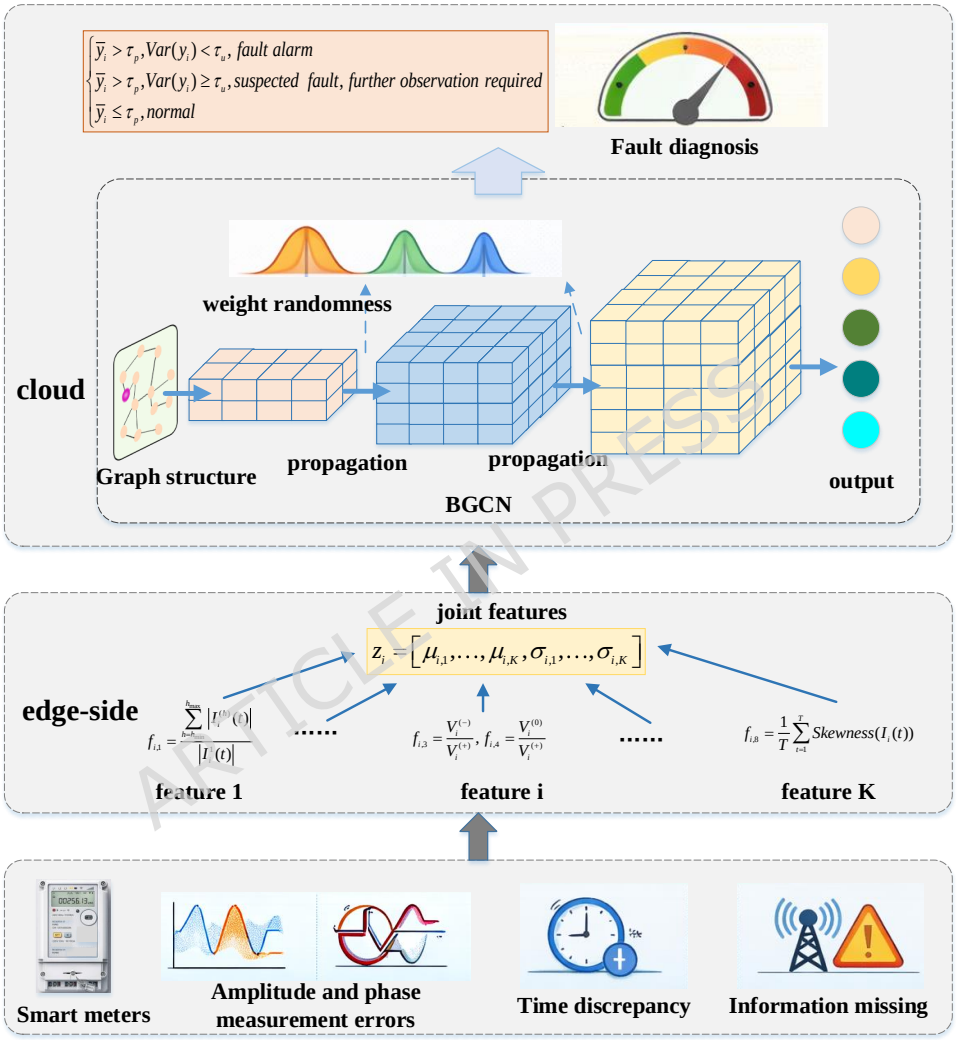

Figure 1. The overall flowchart of the ECCFD method.

Table 2. Leakage-safe event-based data splitting protocol for simulation platform data.

Dataset	Split	Normal events (Time blocks)	HIF events	Total windows (Samples)
Simulation	Training (60%)	60	60	15000
(IEEE 33-Bus)	Validation (20%)	20	20	5000
	Testing (20%)	20	20	5000

Table 3. Sensitivity analysis of τ_p and τ_u combinations on simulation data ($\sigma = 5\%$).

τ_p	τ_u	Suspected Ratio (%)	Confirmed Accuracy (%)	False Alarm Rate (FAR) (%)
0.50	0.05	2.8	92.15	3.40
0.50	0.02	5.8	94.80	1.20
0.70	0.05	3.5	93.80	2.50
0.70	0.02	6.2	95.60	0.85
0.90	0.02	8.1	97.50	0.40

confirming the real-time feasibility of the proposed framework for distribution network monitoring. Unless otherwise stated, all hyperparameters (window size T=0.2s, hidden units=64, learning rate=0.005) were kept consistent between the IEEE 33-bus simulation and the actual field data experiments to demonstrate the robustness and transferability of the proposed ECCFD framework. The measurement metrics used to evaluate the method performance are as follows: accuracy, recall, precision, and $F1_{score}$.

$$Accuracy = \frac{TP+TN}{TP+FP+TN+FN} \times 100\% \tag{46}$$

$$Precision = \frac{TP}{TP+FP} \times 100\% \tag{47}$$

$$Recall = \frac{TP}{TP+FN} \times 100\% \tag{48}$$

$$F1_{score} = \frac{2 \times Precision \times Recall}{Precision + Recall} \tag{49}$$

where TP and TN represent the number of correctly predicted samples, while FP and FN represent the number of incorrectly predicted samples.

1) Sensitivity analysis of τ_p and τ_u combinations on simulation data ($\sigma = 5\%$)

The sensitivity analysis on the simulation dataset (Table 3) demonstrates the critical interplay between the probability threshold (τ_p) and the cognitive uncertainty gate (τ_u) under controlled high-noise conditions ($\sigma = 5\%$). When a lenient uncertainty gate ($\tau_u = 0.05$) is paired with a standard classification boundary ($\tau_p = 0.50$), the false alarm rate (FAR) remains at 3.40%, indicating that a portion of noise-corrupted samples are still misclassified as confirmed faults. However, by tightening the uncertainty threshold to ($\tau_u = 0.02$), the system actively intercepts 5.8% of highly ambiguous predictions. This selective interception effectively halves the FAR to 1.20% while elevating the Confirmed Accuracy to 94.80%. Furthermore, the results reveal that attempting to reduce false alarms by solely increasing the base probability threshold (e.g., $\tau_p = 0.90$) makes the classifier overly conservative, leading to excessive sample rejection (8.1%) and a potential loss of sensitivity to weak HIF signatures. Thus, the combination of ($\tau_p = 0.50$, $\tau_u = 0.02$) provides an optimal operational balance between sensitivity and reliability.

2) Robustness verification under different fault resistors

Each fault resistor was configured to generate 500 test samples for each type of resistor $R_f \in \{200, 500, 1000, 1500, 2000\}\,\Omega$. The proposed BGCN method was compared with traditional methods such as extracting artificial features + support vector machine (SVM)[37], convolutional neural network (CNN), GCN, and graph attention network (GAT)[38]. All comparison methods are based on ensuring strict input parity (same features, same topology where applicable). The comparison results are shown in the Table 4 and Fig.2.

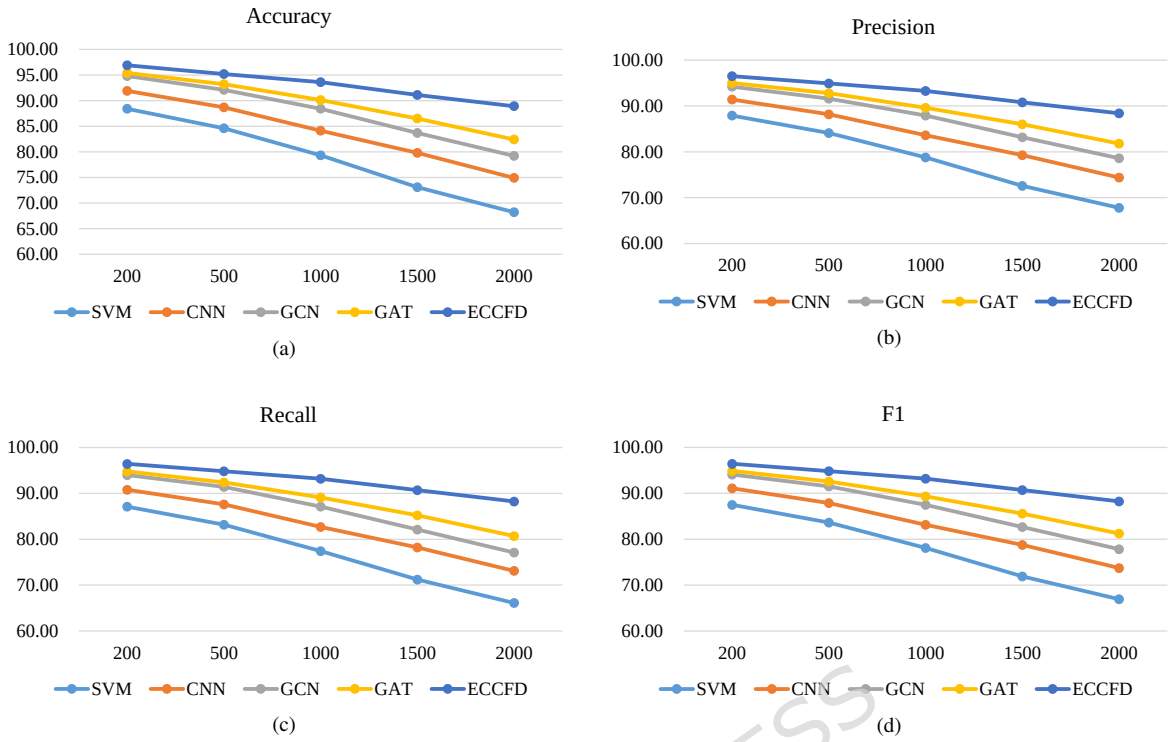

Figure 2. (a) The accuracy of algorithms under different fault resistors for simulation platform data; (b) The precision of algorithms under different fault resistors for simulation platform data; (c) The recall of algorithms under different fault resistors for simulation platform data; (d) The $F1_{score}$ of algorithms under different fault resistors for simulation platform data.

As the fault resistance increases, the electrical disturbances caused by HIFs gradually weaken, and the recognition performance of all methods declines. Traditional SVM and CNN, relying on local features or temporal patterns, struggle to effectively distinguish between faults and normal operating conditions under high fault resistance. GCN and GAT significantly improve overall performance by introducing distribution network topology information, with GAT outperforming GCN under medium resistance conditions, indicating that the attention mechanism can alleviate feature weakening to some extent. However, in the high resistance region ($R_f \geq 1500\Omega$), the performance degradation of deterministic models remains significant. In contrast, the proposed ECCFD maintains the highest accuracy and F1 score under all fault resistance conditions, demonstrating that its uncertainty modeling can more effectively suppress the adverse effects of weak features.

3) Stability verification experiment under different measurement noise levels

To verify the stability of the proposed method under different measurement noise levels $\sigma = \{0\%, 1\%, 3\%, 5\%\}$, ECCFD was compared with SVM, CNN, GCN, and GAT. It should be noted that the scenarios where $\sigma = 3\%$ and $\sigma = 5\%$ are stress testing scenarios. The comparison results are shown in the Table 5 and Fig.3. As the measurement noise level increases, the fault identification performance of all methods declines to varying degrees. SVM and CNN are the most sensitive to noise, exhibiting the fastest performance degradation. GCN and GAT, by introducing the distribution network topology, demonstrate better stability under low to medium noise conditions, but are still inevitably affected under high noise levels. Compared to GCN, GAT achieves better accuracy and F1 scores across all noise levels, indicating that the attention mechanism can adaptively adjust the importance of neighboring nodes to some extent, thereby mitigating the impact of local noise propagation. However, since the model parameters remain deterministic, its performance still significantly decreases under high noise conditions. The proposed ECCFD consistently maintains the highest identification performance across different noise levels, especially under high noise conditions (5%), where its $F1_{score}$ is still approximately 5.5% higher than GAT. This demonstrates that introducing uncertainty modeling at the model parameter level can effectively mitigate the negative impact of measurement noise on feature propagation and the decision-making process, thereby significantly improving the model's stability and reliability under complex operating conditions.

4) Uncertainty calibration and reliability analysis

To rigorously evaluate the reliability of the probabilistic outputs generated by the proposed ECCFD framework compared to state-of-the-art baselines, this section conducted calibration analysis under the most challenging experimental condition:

Table 4. Comparison results of algorithms under different fault resistors for simulation platform data.

Accuracy (%)						Recall (%)					
Alg\Rf	200	500	1000	1500	2000	Alg\Rf	200	500	1000	1500	2000
SVM	88.40	84.60	79.30	73.10	68.20	SVM	87.10	83.20	77.40	71.20	66.10
CNN	91.90	88.70	84.10	79.80	74.90	CNN	90.80	87.60	82.70	78.20	73.10
GCN	94.80	92.10	88.40	83.70	79.20	GCN	94.00	91.40	87.10	82.10	77.10
GAT	95.40	93.20	90.10	86.50	82.40	GAT	94.80	92.40	89.10	85.20	80.70
ECCFD	96.90	95.20	93.60	91.10	88.90	ECCFD	96.45	94.85	93.20	90.70	88.25
Precision (%)						$F1_{score}$ (%)					
Alg\Rf	200	500	1000	1500	2000	Alg\Rf	200	500	1000	1500	2000
SVM	87.90	84.10	78.80	72.60	67.80	SVM	87.50	83.65	78.09	71.89	66.94
CNN	91.40	88.20	83.60	79.30	74.40	CNN	91.10	87.90	83.15	78.75	73.74
GCN	94.20	91.60	87.90	83.20	78.60	GCN	94.10	91.50	87.50	82.65	77.84
GAT	95.00	92.80	89.60	86.00	81.80	GAT	94.90	92.60	89.35	85.60	81.25
ECCFD	96.50	94.90	93.30	90.80	88.40	ECCFD	96.45	94.85	93.20	90.70	88.25

Figure 3. (a) The accuracy of algorithms under different measurement noise levels for simulation platform data; (b) The precision of algorithms under different measurement noise levels for simulation platform data; (c) The recall of algorithms under different measurement noise levels for simulation platform data; (d) The $F1_{score}$ of algorithms under different measurement noise levels for simulation platform data.

Table 5. Comparison results of algorithms under different measurement noise levels for simulation platform data.

Accuracy (%)					Recall (%)				
Alg\σ	0%	1%	3%	5%	Alg\σ	0%	1%	3%	5%
SVM	87.60	83.90	78.10	72.80	SVM	86.20	82.40	76.30	70.90
CNN	90.80	87.10	82.60	77.40	CNN	89.60	85.90	81.10	75.60
GCN	93.20	90.10	86.00	81.80	GCN	92.30	89.10	84.70	80.20
GAT	94.10	91.70	88.40	84.20	GAT	93.20	90.70	87.10	82.60
ECCFD	95.60	94.00	92.10	89.30	ECCFD	94.80	93.10	91.20	88.20
Precision (%)					$F1_{score}$ (%)				
Alg\σ	0%	1%	3%	5%	Alg\σ	0%	1%	3%	5%
SVM	86.90	83.20	77.40	72.10	SVM	86.55	82.80	76.85	71.49
CNN	90.20	86.50	81.90	76.80	CNN	89.90	86.20	81.50	76.20
GCN	92.70	89.60	85.40	81.10	GCN	92.50	89.35	85.05	80.65
GAT	93.60	91.20	87.80	83.50	GAT	93.40	90.95	87.45	83.05
ECCFD	95.20	93.60	91.70	88.80	ECCFD	95.00	93.35	91.45	88.50

Table 6. Calibration performance comparison.

Alg	ECE (overall)	Bin 1 Acc (0.5-0.6]	Bin 2 Acc (0.6-0.7]	Bin 3 Acc (0.7-0.8]	Bin 4 Acc (0.8-0.9]	Bin 1 Acc (0.9-1.0]
SVM	0.22	0.35	0.42	0.50	0.60	0.75
CNN	0.18	0.40	0.48	0.55	0.66	0.80
GCN	0.12	0.41	0.49	0.56	0.68	0.83
GAT	0.08	0.48	0.56	0.65	0.76	0.90
ECCFD	0.03	0.53	0.64	0.74	0.84	0.96

simulation platform with high measurement noise (σ=5%). Under this condition, the measurement data is significantly corrupted by amplitude error, phase noise, and time asynchrony. We used the expected calibration error (ECE) with M=5 uniform bins to quantify the alignment between predicted confidence and actual accuracy. A lower ECE indicates a more reliable model that is neither over-confident nor under-confident.

$$ECE = \sum_{m=1}^{M} \frac{|B_m|}{N} |acc(B_m) - conf(B_m)| \tag{50}$$

where M is the number of class, B_m is the number of samples in the m-th group, N is the total number of samples, $acc(B_m)$ is the actual accuracy rate of this group, $conf(B_m)$ is the average confidence level of this group.

As shown in Table 6, traditional methods (SVM and CNN) exhibit high ECE values (0.22 and 0.18, respectively). In the highest confidence bin (0.9-1.0), although these models predict with near-certainty, their actual accuracy drops below 80%. This indicates severe over-confidence, likely due to overfitting on noisy local features without accounting for global topology or uncertainty. Graph-based deterministic methods (GCN and GAT) show improved calibration (ECE 0.12 and 0.08), benefiting from topological information smoothing. However, they still suffer from over-confidence in high-noise scenarios because their fixed weights cannot express epistemic uncertainty. For instance, GCN assigns high probability to noisy samples that are actually misclassified (Bin 5 accuracy only 83%).

In contrast, the proposed ECCFD achieves a significantly lower ECE of 0.03. The gap between confidence and accuracy is consistently small across all bins. This demonstrates that by integrating metering uncertainty into the Bayesian learning process via variational inference, the model's output probabilities are well-calibrated. When the input is noisy or ambiguous, the Bayesian network naturally lowers its confidence, aligning its predictions with the true likelihood of correctness.

To verify the unique utility of the proposed Bayesian uncertainty for decision-making, we analyzed the statistical relationship between prediction error and predictive variance for the ECCFD model. The distribution of predictive variance for correctly classified vs. misclassified samples is summarized in Table 7. Fig.4 shows reliability/ECE and error–uncertainty correlation.The results indicate a strong correlation between prediction error and uncertainty. The mean uncertainty of misclassified samples (0.04) is 10 times higher than that of correctly classified samples (0.00). This significant margin confirms that high predictive uncertainty is a robust indicator of potential misclassification. Unlike deterministic baselines (SVM/CNN/GCN/GAT) which

Table 7. Uncertainty statistics for correct vs. incorrect predictions (ECCFD).

Prediction group	Mean uncertainty	Std. Dev.	Median	Max value
Correct predictions	0.00	0.00	0.00	0.01
Incorrect predictions	0.04	0.02	0.04	0.09
Ratio(inc/corr)	10.00	-	13.33	9.00

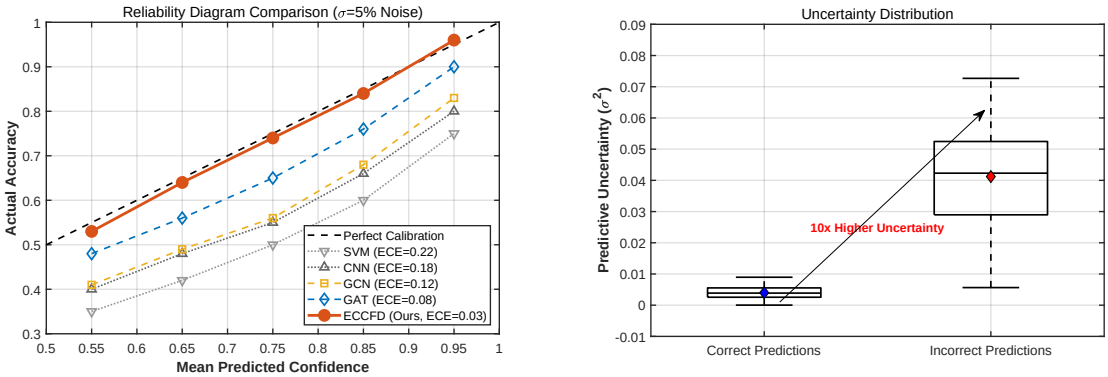

Figure 4. (a) Calibration performance comparison; (b) Uncertainty statistics for correct vs. incorrect predictions (ECCFD);

only output probability scores, ECCFD provides this additional uncertainty metric, enabling the system to effectively filter out unreliable predictions and suppress false alarms caused by measurement noise.

While ECE and variance correlation demonstrate excellent probabilistic calibration, they do not explicitly quantify the operational benefits of uncertainty gating. To directly measure how uncertainty improves practical decision-making trade-offs, we evaluated the Coverage-Accuracy (Selective Risk) curve on the high-noise (σ=5%) simulation dataset. In this decision-centric metric, the model is allowed to abstain from predicting (i.e., routing to the "suspected fault" state) a certain percentage of the most uncertain samples. We rank all test samples by their predictive variance (epistemic uncertainty) and incrementally reject the top x% most uncertain samples. The operational accuracy is then calculated on the remaining (retained) samples. As shown in Table 8, there is a strong monotonic relationship between sample rejection and system accuracy. Without uncertainty gating (0% rejected), the baseline accuracy is 89.30% with an unacceptable FAR of 5.90%. However, by selectively rejecting just the top 5% of the most uncertain samples (routing them for manual observation), the operational accuracy jumps significantly to 93.80%, and the FAR plummets to 1.80%. If the operational constraint is exceedingly strict, rejecting the top 15% pushes the accuracy to 98.10% with a near-zero FAR. This direct quantification definitively proves that the Bayesian predictive variance is not merely a well-calibrated statistical metric, but a highly effective, decision-centric operational tool. It allows grid operators to actively trade off a small fraction of automated coverage to drastically mitigate selective risk and prevent false disconnections under severe measurement noise.

5) The impact of uncertainty-aware alarms on false alarms and missed alarms

Using new data, we compared the ECCFD model and the GAT algorithm with BGCNW (which does not have uncertainty-

Table 8. Coverage-accuracy operational trade-off based on uncertainty rejection.

Rejected ratio (Top x% uncertain samples)	Retained coverage (%)	Operational accuracy on retained samples (%)	FAR (%)
0% (No Gating)	100%	89.30	5.90
5%	95%	93.80	1.80
10%	90%	96.50	0.70
15%	85%	98.10	0.20
20%	80%	99.20	0.05

Table 9. Comparison results of uncertainty-aware alarms on false alarms and missed alarms for simulation platform data.

Alg	Accuracy(%)	Precision(%)	Recall(%)	$F1_{score}$ (%)	FPR (%)	FNR (%)
GAT	91.60	91.00	90.40	90.70	9.20	9.60
BGCNW	92.80	92.30	91.90	92.10	7.80	8.10
ECCFD	94.20	94.00	93.60	93.80	5.90	6.40

Table 10. The results of ablation study.

Model Variant	M	E	G	B	Accuracy (%)	Precision (%)	Recall (%)	$F1_{score}$ (%)
Baseline (MLP)	×	×	×	×	64.50	66.80	63.70	65.20
Model 1	√	×	×	×	71.80	73.50	71.50	72.50
Model 2	√	√	×	×	80.50	82.20	80.60	81.40
Model 3	√	√	√	×	86.20	87.50	86.10	86.80
ECCFD	√	√	√	√	89.30	91.40	89.60	90.50

aware alarms), and added evaluation metrics such as false positive rate (FPR) and false negative rate (FNR):

$$FPR = \frac{FP}{FP+TN} \times 100\% \tag{51}$$

$$FNR = \frac{FN}{FN+TP} \times 100\% \tag{52}$$

The Table 9 shows that GAT is prone to misclassifying normal samples as faults under measurement uncertainty, with an FPR as high as 9.2%. BGCNW slightly reduces the false alarm rate to 7.8% by modeling the graph structure. After introducing prediction uncertainty, ECCFD can filter low-confidence samples, reducing the FPR to 5.9%, significantly reducing the probability of false alarms. GAT is affected by measurement errors, and some fault samples are missed, with an FNR of 9.6%. BGCNW reduces this to 8.1%, indicating that graph structure and feature extraction help capture more fault features. Bayesian uncertainty perception further reduces the FNR to 6.4%, indicating that the ability to identify weak fault signals is enhanced. Introducing Bayesian uncertainty not only improves accuracy and F_1score, but also effectively reduces false alarm and missed alarm rates, making fault diagnosis more reliable and suitable for engineering deployment.

6) Ablation study

To rigorously quantify the contribution of each module in the proposed framework, we conducted a systematic ablation study under the challenging high-noise simulation scenario (R_F=2000Ω, σ=5%). We decomposed the ECCFD method into four progressive components: Meter Uncertainty Modeling (M): Incorporating the statistical error model as a data augmentation strategy during training. Edge Feature Processing (E): Using the proposed multi-dimensional feature vector (e.g., harmonic ratios, sequence components) instead of raw measurements. Topology Modeling (G): Utilizing GCN to capture spatial correlations in the distribution network. Bayesian Inference (B): Introducing variational inference (BGCN) for uncertainty quantification. The results are shown in Table 10.

The baseline MLP trained on clean data performs poorly on noisy test data. Introducing the metering uncertainty model (Model 1) significantly improves generalization by exposing the network to realistic noise distributions during training, boosting accuracy to 71.80%. Comparing Model 1 with Model 2, replacing raw measurements with physics-informed edge features yields a substantial gain. This confirms that domain-specific features like harmonic ratios and sequence components are more discriminative for HIFs than raw waveforms, especially under noise. Model 3 introduces the graph structure (GCN), allowing the model to leverage spatial correlations between neighboring nodes. This effectively suppresses local noise spikes, further increasing accuracy to 86.20%. Finally, the full ECCFD model incorporates Bayesian variational inference. By modeling weight uncertainty, it achieves the highest performance across all metrics. The Bayesian mechanism excels in handling ambiguous samples where deterministic models (Model 3) might be over-confident but wrong, demonstrating the critical value of uncertainty quantification in high-noise environments.

7) Robustness under realistic variations

To verify the applicability of the proposed method in real-world scenarios, we conducted additional stress tests concerning communication reliability and load dynamics. Data transmission in low-voltage PLC networks often suffers from packet loss. We modeled this using a Bernoulli erasure channel with loss rates $p \in \{0\%, 5\%, 10\%, 15\%, 20\%\}$. It should be noted that the scenarios where $p = 20\%$ is stress testing scenario. The performance degradation is summarized in Table 11. Results show

Table 11. Performance comparison under different packet loss rates.

Packet Loss Rate (p)	0%	5%	10%	15%	20%
Accuracy (%) - ECCFD	89.30	89.10	88.50	86.40	81.20
$F1_{score}$(%) - ECCFD	90.50	90.20	89.60	87.50	82.30
Accuracy (%) - CNN (Base)	77.40	74.80	70.50	64.20	58.10
$F1_{score}$(%)- CNN(Base)	75.95	73.20	69.10	62.80	56.40

Table 12. Performance under different load fluctuation levels.

Load Fluctuation (δ)	0%	$\pm$10%	$\pm$20%	$\pm$30%
Accuracy (%)	89.30	89.10	88.50	87.20
$F1_{score}$ (%)	90.50	90.20	89.60	88.10
Precision (%)	91.40	91.10	90.50	89.20
Recall (%)	89.60	89.30	88.70	87.00

that the ECCFD method exhibits strong resilience to data loss. Even at 10% packet loss, the $F1_{score}$ remains high (89.60%), whereas the baseline CNN drops below 70.00%. This robustness is attributed to the graph convolution mechanism, which aggregates information from neighboring nodes to compensate for missing local data. However, when packet loss exceeds 15%, the graph structure becomes too sparse, leading to a significant performance decline.

We introduced random load scaling factors $\delta \in \{0\%, \pm 10\%, \pm 20\%, \pm 30\%\}$ to the simulation. The results are summarized in Table 12. The results indicate that the proposed method is highly insensitive to load changes. Even under $\pm$30% fluctuation, the accuracy drop is minimal. This stability validates the design of our normalized feature vector, which effectively decouples fault characteristics from load magnitude.

8) Scalability analysis on IEEE 123-bus system

To evaluate the scalability of the proposed method, we extended the experiments to the IEEE 123-bus distribution feeder, a larger and more complex radial network. The fault simulation settings remained consistent with the 33-bus case ($\sigma = 0.5$). The results are shown in Table 13. As the system scale increases from 33 to 123 nodes, the fault propagation characteristics become more complex. Traditional data-driven methods (SVM and CNN) struggle to capture these long-range dependencies, showing a significant performance drop. GCN and GAT leverage the topological structure to aggregate neighborhood information, maintaining acceptable performance even in large-scale networks. GAT slightly outperforms GCN due to its attention mechanism focusing on relevant neighbors. The proposed ECCFD framework achieves the highest accuracy of 88.60%, outperforming the second-best method (GAT) by 5.8%. This demonstrates that incorporating metrological uncertainty modeling and Bayesian inference is crucial for reliable fault diagnosis in large-scale, noisy distribution networks. The scalability of our graph-based approach is thus validated.

Verification using actual field data

To verify the generalization ability and practical application performance of the proposed method, this section uses field data collected from smart meters in a city's low-voltage distribution network. The sampling frequency is 2kHz, covering 33 distribution nodes, with a continuous sampling period of two weeks, collecting data 24 hours a day. The measured variables include $\tilde{V}_i(t)$, $\tilde{I}_i(t)$, $\tilde{\phi}_i(t)$. The meter measurements exhibit actual errors: transformer error $\pm$0.5%, clock asynchrony $\pm$1 ms, significant load fluctuations, and large seasonal/time-period differences. The fault events were confirmed through a combination of fault recorder logs, user reports, and on-site maintenance records. The dataset contains 14 confirmed HIF events verified by maintenance logs. The leakage-safe event-based data splitting protocol for simulation platform data is shown in Table 14. Additionally, while field data inherently contains some measurement noise, its magnitude is uncontrolled. To rigorously

Table 13. Performance comparison on IEEE 123-bus system.

Alg	Accuracy (%)	Precision (%)	Recall (%)	$F1_{score}$(%)
SVM	68.50	70.20	65.80	67.90
CNN	74.20	75.80	71.50	73.60
GCN	80.50	82.10	78.40	80.20
GAT	82.80	84.50	80.60	82.50
ECCFD	88.60	89.80	87.20	88.50

Table 14. Leakage-safe event-based data splitting protocol for actual field data.

Dataset	Split	Normal Events (Time Blocks)	HIF Events	Total Windows (Samples)
Field Data	Training (60%)	12 days	8	5040
(2-Week)	Validation (20%)	4 days	3	1680
	Testing (20%)	4 days	3	1680

Table 15. Sensitivity analysis of τ_p and τ_u combinations on platform data ($\sigma = 5\%$).

τ_p	τ_u	Suspected Ratio (%)	Confirmed Accuracy (%)	False Alarm Rate (FAR) (%)
0.50	0.05	2.1	93.10	2.70
0.50	0.02	4.5	95.70	1.10
0.70	0.05	2.9	94.60	1.90
0.70	0.02	5.3	96.80	0.70
0.90	0.02	7.6	98.20	0.30

evaluate the algorithm's robustness under specific degradation levels, we adopted an offline injection strategy. We superimposed additional synthetic noise (Gaussian amplitude/phase errors, random time shifts, and packet loss masks) onto the raw field measurements. This methodology ensures a consistent and reproducible evaluation environment across all compared methods.

1) Sensitivity analysis of τ_p and τ_u combinations on actual field data ($\sigma = 5\%$)

The sensitivity analysis on the field dataset (Table 15) further validates the practical deployability of the three-level decision logic in real-world environments. Field measurements inherently contain complex, unmodeled disturbances that challenge deterministic thresholds. As shown, maintaining high base sensitivity ($\tau_p = 0.50$) with a strict uncertainty gate ($\tau_u = 0.02$) successfully suppresses the FAR to 1.10%—a critical requirement for utility dispatchers to prevent "alarm fatigue". Compared to the lenient setting ($\tau_u = 0.05, FAR = 2.70\%$), the stricter gate increases the "suspected ratio" slightly from 2.1% to 4.5%, effectively isolating the noisy field samples that lack sufficient diagnostic confidence. Importantly, across both datasets, shifting to higher probability thresholds ($\tau_p = 0.70 or 0.90$) consistently increases the suspected ratio significantly while providing diminishing returns in FAR reduction. This confirms that the data-driven calibration of τ_u robustly adapts to actual grid conditions, ensuring that automated alarms (Confirmed Accuracy = 95.70%) are highly reliable without sacrificing the detection of genuine anomalies.

2) Robustness verification under different fault resistors

The fault resistances were set to $R_f \in \{200, 500, 1000, 1500, 2000\}\,\Omega$, and the proposed ECCFD method was compared with traditional SVM, CNN, GCN, and GAT. Additionally, to validate the effectiveness of our method against specialized HIF detection techniques, we implemented a wavelet transform with long short-term memory (WTLSTM) model. This model uses discrete wavelet transform to extract time-frequency features and feeds them into an LSTM network, representing a state-of-the-art temporal feature-based approach. And compared our method with the widely used monte carlo dropout GCN (MCDGCN). The MCDGCN has the same architecture as our model but uses dropout. To strictly isolate the contribution of the bayesian mechanism, we compared our method with a capacity-matched deterministic GCN (CMDGCN). Both models have identical architectures and training hyperparameters (learning rate, epochs), ensuring a fair comparison. The comparison results are shown in the Table 16 and Fig.5.

The comparison results show that as the fault resistance increases, the characteristics of high-resistance faults weaken, and the performance of SVM and CNN declines significantly. GCN utilizes topology to improve recognition capabilities, while the GAT attention mechanism further enhances robustness under medium fault resistance. ECCFD maintains high performance; compared to GAT, ECCFD shows a significant performance improvement (approximately 3%-5%) under high-resistance conditions, demonstrating the ability of uncertainty modeling to suppress the influence of weak features.

3) Stability verification experiment under different measurement noise levels

Consistent with simulation data validation, this section sets the standard deviation of measurement noise to verify the stability of the proposed method under different measurement noise levels $\sigma = \{0\%, 1\%, 3\%, 5\%\}$, comparing ECCFD with SVM, CNN, GCN, and GAT. The comparison results are shown in the Table 17 and Fig.6.

The results show that the performance of all methods decreases with increasing measurement noise, with SVM and CNN being particularly sensitive to noise. GCN and GAT mitigate some of the noise impact through graph structures, with GAT slightly outperforming GCN under low-noise conditions. Under different noise levels, the performance degradation of ECCFD is significantly less than that of CNN and GCN, indicating that Bayesian modeling effectively mitigates the impact of measurement noise. Although the introduced WTLSTM (HIF-oriented temporal baseline) outperforms standard CNNs by effectively capturing time-frequency features (achieving 79.50% accuracy at 5% noise), it still lags behind graph-based

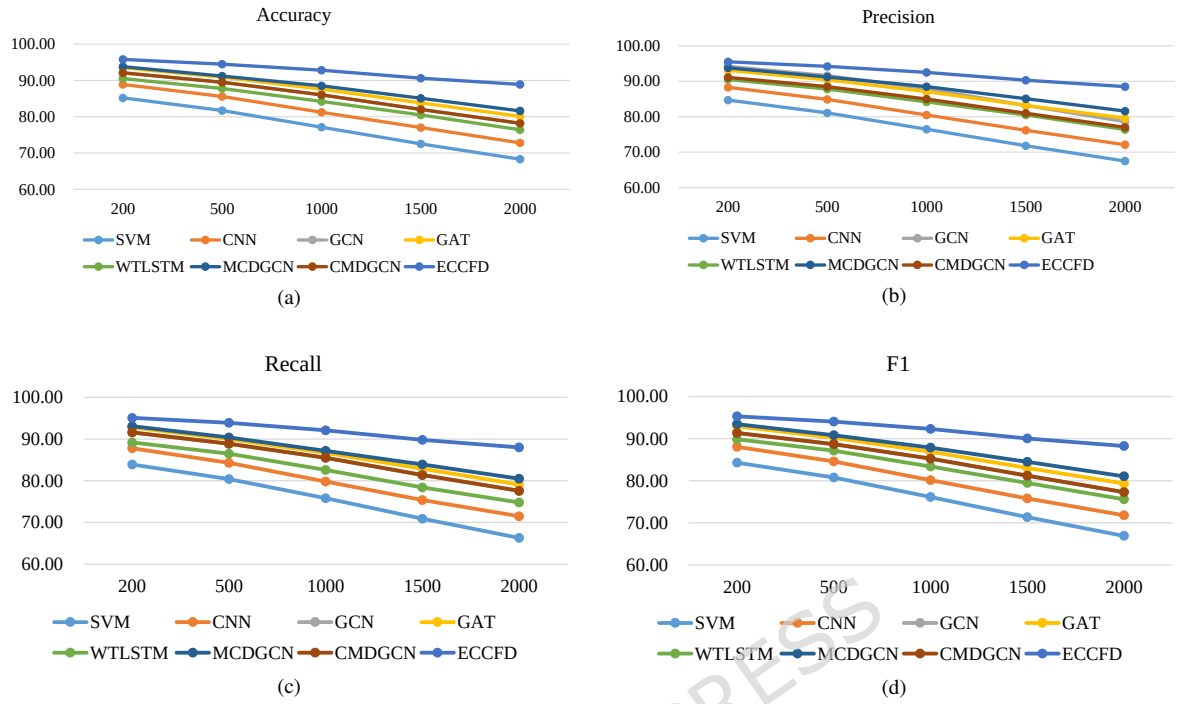

Figure 5. (a) The accuracy of algorithms under different fault resistors for actual field data; (b) The precision of algorithms under different fault resistors for actual field data; (c) The recall of algorithms under different fault resistors for simulation platform data; (d) The $F1_{score}$ of algorithms under different fault resistors for actual field data.

Table 16. Comparison results of algorithms under different fault resistors for actual field data.

Accuracy (%)						Recall (%)					
Alg\Rf	200	500	1000	1500	2000	Alg\Rf	200	500	1000	1500	2000
SVM	85.20	81.70	77.10	72.50	68.30	SVM	83.90	80.40	75.80	70.90	66.30
CNN	88.90	85.60	81.20	77.00	72.80	CNN	87.80	84.30	79.80	75.40	71.50
GCN	92.10	89.50	86.00	82.00	78.20	GCN	91.60	88.90	85.50	81.40	77.60
GAT	93.50	90.90	87.60	83.80	80.10	GAT	92.80	90.00	86.70	82.90	79.10
WTLSTM	90.50	87.80	84.20	80.50	76.40	WTLSTM	89.20	86.50	82.60	78.40	74.80
MCDGCN	93.80	91.20	88.50	85.10	81.60	MCDGCN	93.10	90.40	87.20	83.90	80.50
CMDGCN	92.10	89.50	86.00	82.00	78.20	CMDGCN	91.60	88.90	85.50	81.40	77.60
ECCFD	95.80	94.50	92.80	90.60	88.90	ECCFD	95.10	93.90	92.10	89.80	88.00
Precision (%)						$F1_{score}$ (%)					
Alg\	200	500	1000	1500	2000	Alg\Rf	200	500	1000	1500	2000
SVM	84.70	81.10	76.50	71.80	67.50	SVM	84.30	80.75	76.15	71.35	66.90
CNN	88.30	84.90	80.50	76.20	72.10	CNN	88.05	84.60	80.15	75.80	71.80
GCN	94.20	91.60	87.90	83.20	78.60	GCN	91.35	88.70	85.25	81.20	77.30
GAT	93.10	90.40	87.10	83.20	79.60	GAT	92.95	90.20	86.90	83.05	79.35
WTLSTM	90.50	87.80	84.20	80.50	76.40	WTLSTM	89.85	87.15	83.40	79.45	75.60
MCDGCN	93.80	91.20	88.50	85.10	81.60	MCDGCN	93.45	90.80	87.85	84.50	81.05
CMDGCN	91.10	88.50	85.00	81.00	77.00	CMDGCN	91.35	88.70	85.25	81.20	77.30
ECCFD	95.50	94.20	92.50	90.30	88.50	ECCFD	95.30	94.05	92.30	90.05	88.25

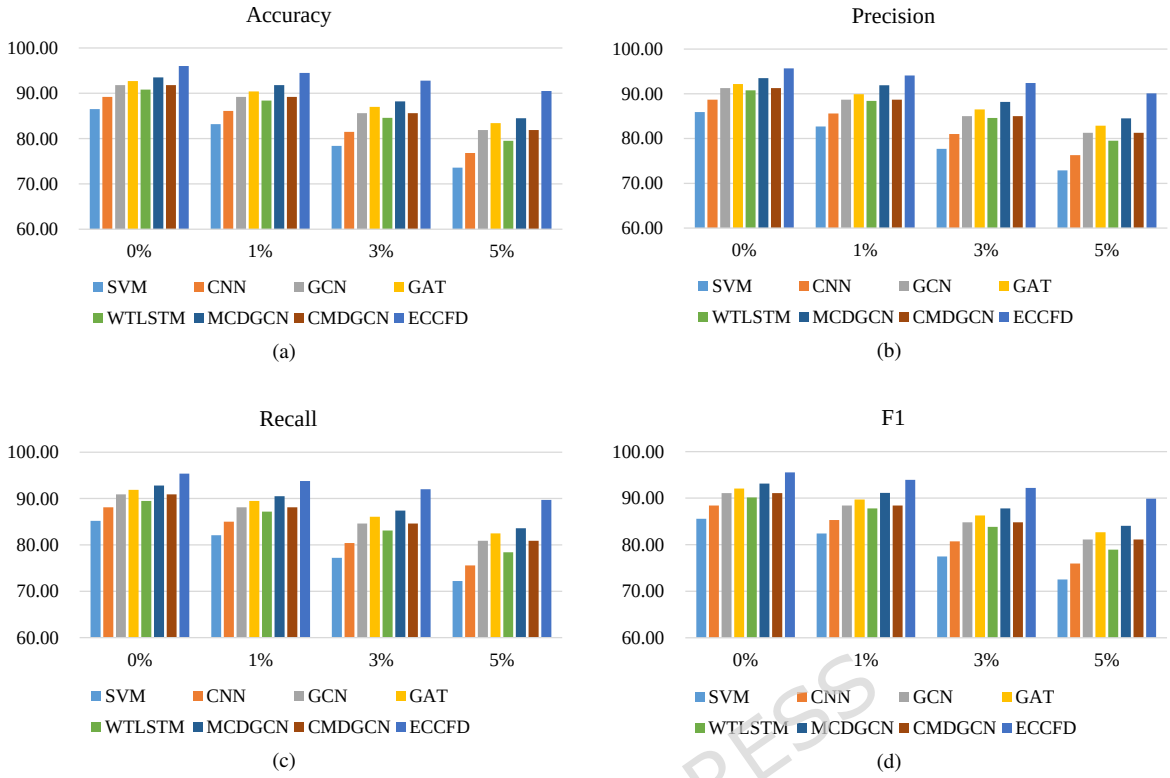

Figure 6. (a) The accuracy of algorithms under different measurement noise levels for actual field data; (b) The precision of algorithms under different measurement noise levels for actual field data; (c) The recall of algorithms under different measurement noise levels for actual field data; (d) The $F1_{score}$ of algorithms under different measurement noise levels for actual field data.

methods (GCN/GAT/ECCFD). This highlights the necessity of incorporating topological constraints for robust diagnosis in distribution networks. The MCDGCN (Uncertainty baseline) demonstrates superior robustness compared to deterministic GCN and GAT, maintaining 84.50% accuracy under high noise. However, the proposed ECCFD still achieves a significant margin (90.50%), confirming that the explicit variational inference framework provides more precise uncertainty estimation than dropout approximation. Meanwhile, under high noise (5%), ECCFD (90.50%) outperforms the CMDGCN (81.90%) by a significant margin of 8.6%, proving that the performance gains stem from the uncertainty modeling rather than model capacity.

4) The impact of uncertainty-aware alarms on false alarms and missed alarms

The ECCFD model and the GAT and BGCNW algorithms (which do not have uncertainty-aware alarms) are compared, and the results are shown in the Table 18. The results show that for the deterministic methods GAT and BGCNW, the models typically make fault judgments directly based on a single forward inference result. When measurement data is affected by transformer errors, communication noise, or load fluctuations, the models are prone to overconfident predictions of boundary samples, leading to a simultaneous increase in both false alarm and false negative rates. In contrast, the uncertainty-aware ECCFD, which incorporates Bayesian modeling, not only outputs fault judgment results but also quantifies prediction uncertainty. When the cognitive uncertainty corresponding to the prediction result is high, the system can mark the sample as a "low-confidence alarm" or delay the decision, effectively avoiding erroneous triggering caused by measurement uncertainty. Experimental results show that, at the same recall level, the false alarm rate of ECCFD is significantly lower than that of non-Bayesian methods, indicating that it can effectively suppress false alarms under normal operating conditions.

On the other hand, in cases of high-impedance faults or weak signal characteristics, traditional methods are more prone to false negatives. The uncertainty perception mechanism, by statistically analyzing multiple Monte Carlo predictions, can identify potentially high-risk samples. Even if the confidence of a single prediction is insufficient, uncertainty aggregation can increase the probability of fault detection. Therefore, ECCFD also shows a significant reduction in the false negative rate on real-world field datasets, demonstrating its stronger sensitivity to weak fault scenarios.

5) Per-event analysis and external validity

Table 17. Comparison results of algorithms under different measurement noise levels for actual field data.

Accuracy (%)					Recall (%)				
Alg\σ	0%	1%	3%	5%	Alg\σ	0%	1%	3%	5%
SVM	86.50	83.20	78.40	73.60	SVM	85.20	82.10	77.20	72.20
CNN	89.20	86.10	81.50	76.80	CNN	88.10	85.00	80.40	75.60
GCN	91.80	89.20	85.60	81.90	GCN	90.90	88.10	84.60	80.90
GAT	92.70	90.40	87.00	83.40	GAT	91.90	89.50	86.10	82.50
WTLSTM	90.80	88.40	84.60	79.50	WTLSTM	89.50	87.20	83.10	78.40
MCDGCN	93.50	91.80	88.20	84.50	MCDGCN	92.80	90.50	87.40	83.60
CMDGCN	91.80	89.20	85.60	81.90	CMDGCN	90.90	88.10	84.60	80.90
ECCFD	96.00	94.50	92.80	90.50	ECCFD	95.40	93.80	92.00	89.70
Precision (%)					$F1_{score}$ (%)				
Alg\σ	0%	1%	3%	5%	Alg\σ	0%	1%	3%	5%
SVM	85.90	82.70	77.70	72.90	SVM	85.55	82.40	77.45	72.55
CNN	88.70	85.60	81.00	76.30	CNN	88.40	85.30	80.70	75.95
GCN	91.30	88.70	85.00	81.30	GCN	91.10	88.40	84.80	81.10
GAT	92.20	89.90	86.50	82.90	GAT	92.05	89.70	86.30	82.70
WTLSTM	90.80	88.40	84.60	79.50	WTLSTM	90.15	87.80	83.85	78.95
MCDGCN	93.50	91.90	88.20	84.50	MCDGCN	93.15	91.15	87.80	84.05
CMDGCN	91.30	88.70	85.00	81.30	CMDGCN	91.10	88.40	84.80	81.10
ECCFD	95.70	94.10	92.40	90.10	ECCFD	95.55	93.95	92.20	89.90

Table 18. Comparison results of uncertainty-aware alarms on false alarms and missed alarms for actual field data.

Alg	Accuracy(%)	Precision(%)	Recall(%)	$F1_{score}$ (%)	FPR (%)	FNR (%)
GAT	91.5	90.9	90.3	90.6	9.3	9.7
BGCNW	92.7	92.1	91.8	91.95	7.9	8.2
ECCFD	94.1	93.8	93.5	93.65	5.9	6.4

To evaluate the practical deployability of the proposed ECCFD framework in real-world urban environments, we extended our assessment from window-level metrics to event-level analysis. The field dataset, spanning an intensive two-week monitoring period, contains 14 confirmed high-impedance fault (HIF) events. Unlike medium-voltage overhead networks where HIFs typically result from downed conductors on soil or asphalt, the confirmed events in our low-voltage smart meter dataset exhibit distinct urban characteristics. Specifically, the events encompass intermittent arcing caused by insulation degradation at underground cable joints (6 instances), tree branches contacting exposed overhead service drops (4 instances), and high-resistance heating due to poor or corroded connections in street-level distribution cabinets (4 instances). These events occurred across diverse topological locations—ranging from main feeder branches to individual service lines—and during varied operating regimes, including peak load periods (e.g., 18:00) with high current stress and light load periods (e.g., 03:00) exacerbated by moisture condensation.

During the rigorous 4-day testing phase, which included 3 distinct and diverse HIF episodes, the proposed ECCFD model successfully detected all events, achieving a 100% event-level hit rate. Furthermore, when evaluated over continuous normal operating periods to assess false alarm robustness, the model generated only 0.5 false alarms per day (i.e., 2 isolated false-positive windows over 96 hours). This exceptionally low false alarm rate, achieved through the Bayesian cognitive uncertainty gating mechanism, confirms that the system is highly reliable and meets the stringent operational requirements of LV distribution network dispatchers without causing alarm fatigue.

Conclusions

To address the challenges of weak high-resistance fault characteristics in low-voltage distribution networks, susceptibility to measurement errors and environmental noise, and insufficient robustness of existing methods in practical deployments, this paper systematically studies an ECCFD method based on the non-ideal measurement characteristics of smart meters. First, to address the common problems of amplitude error, phase deviation, time asynchrony, and communication instability in low-cost smart meters, a unified statistical model of measurement uncertainty is established, providing a foundation for subsequent feature extraction and probabilistic inference. Second, multi-dimensional information such as higher harmonic ratios, sequence components, and statistical characteristics are fused at the edge side, effectively enhancing the separability of weak high-resistance fault characteristics and reducing the interference of load fluctuations on diagnostic results. Finally,

BGCN is introduced in the cloud to explicitly integrate measurement uncertainty into the model parameter distribution. Through variational inference and Monte Carlo prediction, a joint output of fault probability and cognitive uncertainty is achieved. Multiple experimental verifications based on standard IEEE distribution system test networks and actual field datasets demonstrate that the proposed method exhibits excellent diagnostic performance under different fault resistances and measurement noise levels. Meanwhile, the uncertainty-aware alarm mechanism significantly reduces the false alarm rate and false negative rate, making fault diagnosis results more reliable and robust. Even at a noise level of 5%, ECCFD can achieve an accuracy of 89.30% and 90.50% respectively. Considering that the actual distribution network topology may change with operating conditions, future research can explore dynamic GNNs and online Bayesian update mechanisms to achieve the model's adaptive capability to network topology changes and operating condition evolution.

Data availability

The datasets analysed during the current study are available from the corresponding author on reasonable request.

References

1. Sapountzoglou, N., Lago, J., De Schutter, B. & Raison, B. A generalizable and sensor-independent deep learning method for fault detection and location in low-voltage distribution grids. *Appl. Energy* **276**, 115299, DOI: 10.1016/j.apenergy.2020.115299 (2020).

2. Penido, D. R. R., de Araujo, L. R., Rodrigues, V. T. S. & do Nascimento, K. B. An Analytical Zero Sequence Method to Locate Fault in Distribution Systems Rich in DG. *IEEE Transactions on Smart Grid* **13**, 1849–1859, DOI: 10.1109/TSG.2022.3141207 (2022).

3. Oh, Y.-S. *et al.* Fault detection scheme based on mathematical morphology in last mile radial low voltage DC distribution networks. *Int. J. Electr. Power & Energy Syst.* **106**, 520–527, DOI: 10.1016/j.ijepes.2018.10.035 (2019).

4. Depuru, S. S. S. R., Wang, L. & Devabhaktuni, V. Smart meters for power grid: Challenges, issues, advantages and status. *Renew. Sustain. Energy Rev.* **15**, 2736–2742, DOI: 10.1016/j.rser.2011.02.039 (2011).

5. Wen, L., Zhou, K., Yang, S. & Li, L. Compression of smart meter big data: A survey. *Renew. Sustain. Energy Rev.* **91**, 59–69, DOI: 10.1016/j.rser.2018.03.088 (2018).

6. Uribe-Pérez, N., Hernández, L., De la Vega, D. & Angulo, I. State of the Art and Trends Review of Smart Metering in Electricity Grids. *Appl. Sci.* **6**, 68, DOI: 10.3390/app6030068 (2016). Publisher: Multidisciplinary Digital Publishing Institute.

7. Baharozu, E., Ilhan, S. & Soykan, G. High impedance fault localization: A comprehensive review. *Electr. Power Syst. Res.* **214**, 108892, DOI: 10.1016/j.epsr.2022.108892 (2023).

8. Ghaderi, A., Ginn, H. L. & Mohammadpour, H. A. High impedance fault detection: A review. *Electr. Power Syst. Res.* **143**, 376–388, DOI: 10.1016/j.epsr.2016.10.021 (2017).

9. Aljohani, A. & Habiballah, I. High-Impedance Fault Diagnosis: A Review. *Energies* **13**, 6447, DOI: 10.3390/en13236447 (2020). Publisher: Multidisciplinary Digital Publishing Institute.

10. Yang, C., Zhang, W., Tang, R. & Xiao, X. Tree-Related High-Impedance Fault in Distribution Systems: Modeling, Detection, and Ignition Risk Assessment (Review). *Energies* **18**, 548, DOI: 10.3390/en18030548 (2025). Publisher: Multidisciplinary Digital Publishing Institute.

11. Mishra, M. & Panigrahi, R. R. Taxonomy of high impedance fault detection algorithm. *Measurement* **148**, 106955, DOI: 10.1016/j.measurement.2019.106955 (2019).

12. Huaquisaca Paye, J. C. *et al.* High Impedance Fault Models for Overhead Distribution Networks: A Review and Comparison with MV Lab Experiments. *Energies* **17**, 1125, DOI: 10.3390/en17051125 (2024). Publisher: Multidisciplinary Digital Publishing Institute.

13. Costa, M. M., Martinez, M. A. G. & Costa, J. C. W. A. Review of Uncertainty Sources in Optical Current Sensors Used in Power Systems. *Energies* **17**, 4162, DOI: 10.3390/en17164162 (2024). Publisher: Multidisciplinary Digital Publishing Institute.

14. Raghuvamsi, Y. & Teeparthi, K. A review on distribution system state estimation uncertainty issues using deep learning approaches. *Renew. Sustain. Energy Rev.* **187**, 113752, DOI: 10.1016/j.rser.2023.113752 (2023).

15. Hadi, M. B., Moeini-Aghtaie, M., Khoshjahan, M. & Dehghanian, P. A Comprehensive Review on Power System Flexibility: Concept, Services, and Products. *IEEE Access* **10**, 99257–99267, DOI: 10.1109/ACCESS.2022.3206428 (2022).

16. Ginzburg-Ganz, E. *et al.* Statistical Foundations of Generative AI for Optimal Control Problems in Power Systems: Comprehensive Review and Future Directions. *Energies* **18**, 2461, DOI: 10.3390/en18102461 (2025). Publisher: Multidisciplinary Digital Publishing Institute.

17. Rahman, M. M., Dadon, S. H., He, M., Giesselmann, M. & Hasan, M. M. An Overview of Power System Flexibility: High Renewable Energy Penetration Scenarios. *Energies* **17**, 6393, DOI: 10.3390/en17246393 (2024). Publisher: Multidisciplinary Digital Publishing Institute.

18. Liu, T., Song, Y., Zhu, L. & Hill, D. J. Stability and Control of Power Grids. *Annu. Rev. Control. Robotics, Auton. Syst.* **5**, 689–716, DOI: 10.1146/annurev-control-042820-011148 (2022). Publisher: Annual Reviews.

19. Hussain, M. T., Sulaiman, D. N. B., Hussain, M. S. & Jabir, M. Optimal Management strategies to solve issues of grid having Electric Vehicles (EV): A review. *J. Energy Storage* **33**, 102114, DOI: 10.1016/j.est.2020.102114 (2021).

20. Zheng, Y., Niu, S., Shang, Y., Shao, Z. & Jian, L. Integrating plug-in electric vehicles into power grids: A comprehensive review on power interaction mode, scheduling methodology and mathematical foundation. *Renew. Sustain. Energy Rev.* **112**, 424–439, DOI: 10.1016/j.rser.2019.05.059 (2019).

21. Talaat, M., Alsayyari, A. S., Alblawi, A. & Hatata, A. Y. Hybrid-cloud-based data processing for power system monitoring in smart grids. *Sustain. Cities Soc.* **55**, 102049, DOI: 10.1016/j.scs.2020.102049 (2020).

22. AL-Jumaili, A. H. A., Mashhadany, Y. I. A., Sulaiman, R. & Alyasseri, Z. A. A. A Conceptual and Systematics for Intelligent Power Management System-Based Cloud Computing: Prospects, and Challenges. *Appl. Sci.* **11**, 9820, DOI: 10.3390/app11219820 (2021). Publisher: Multidisciplinary Digital Publishing Institute.

23. Ahmad, A. B. *et al.* Renewable integration and energy storage management and conversion in grid systems: A comprehensive review. *Energy Reports* **13**, 2583–2602, DOI: 10.1016/j.egyr.2025.02.008 (2025).

24. Ahsan, F. *et al.* Data-driven next-generation smart grid towards sustainable energy evolution: techniques and technology review. *Prot. Control. Mod. Power Syst.* **8**, 1–42, DOI: 10.1186/s41601-023-00319-5 (2023).

25. Lal, M. D. & Varadarajan, R. A Review of Machine Learning Approaches in Synchrophasor Technology. *IEEE Access* **11**, 33520–33541, DOI: 10.1109/ACCESS.2023.3263547 (2023).

26. Yu, J. *et al.* Deep Learning Models for PV Power Forecasting: Review. *Energies* **17**, 3973, DOI: 10.3390/en17163973 (2024). Publisher: Multidisciplinary Digital Publishing Institute.

27. Chung, S. & Zhang, Y. Artificial Intelligence Applications in Electric Distribution Systems: Post-Pandemic Progress and Prospect. *Appl. Sci.* **13**, 6937, DOI: 10.3390/app13126937 (2023). Publisher: Multidisciplinary Digital Publishing Institute.

28. Amangeldy, B., Imankulov, T., Tasmurzayev, N., Dikhanbayeva, G. & Nurakhov, Y. A Review of Artificial Intelligence and Deep Learning Approaches for Resource Management in Smart Buildings. *Buildings* **15**, 2631, DOI: 10.3390/buildings15152631 (2025). Publisher: Multidisciplinary Digital Publishing Institute.

29. Li, Y., Xue, C., Zargari, F. & Li, Y. R. From Graph Theory to Graph Neural Networks (GNNs): The Opportunities of GNNs in Power Electronics. *IEEE Access* **11**, 145067–145084, DOI: 10.1109/ACCESS.2023.3345795 (2023).

30. Guato Burgos, M. F., Morato, J. & Vizcaino Imacaña, F. P. A Review of Smart Grid Anomaly Detection Approaches Pertaining to Artificial Intelligence. *Appl. Sci.* **14**, 1194, DOI: 10.3390/app14031194 (2024). Publisher: Multidisciplinary Digital Publishing Institute.

31. Zhang, J. *et al.* Remaining useful life prediction based on self-attention mechanism -sequential variational autoencoder: From a semi-supervised perspective. *Adv. Eng. Informatics* **71**, 104242, DOI: https://doi.org/10.1016/j.aei.2025.104242 (2026).

32. Zhang, J. *et al.* A transferable topology-aware graph pooling network for remaining useful life prediction under cross-domain conditions. *IEEE Transactions on Reliab.* 1–15, DOI: 10.1109/TR.2025.3643102 (2025).

33. Xu, X. *et al.* A comprehensive review of graph convolutional networks: approaches and applications. *Electron. Res. Arch.* **31**, 4185–4215, DOI: 10.3934/era.2023213 (2023). Cc_license_type: cc_by Primary_atype: Electronic Research Archive Subject_term: Review Subject_term_id: Review.

34. Kipf, T. N. & Welling, M. Semi-supervised classification with graph convolutional networks. *CoRR* **abs/1609.02907**, DOI: https://doi.org/10.48550/arXiv.1609.02907 (2016). 1609.02907.

35. Fisher, R. A. On the mathematical foundations of theoretical statistics. *Philos. Transactions Royal Soc. London. Ser. A, Containing Pap. a Math. or Phys. Character* **222**, 309–368 (1922).

36. Blundell, C., Cornebise, J., Kavukcuoglu, K. & Wierstra, D. Weight uncertainty in neural networks, DOI: https://doi.org/10.48550/arXiv.1505.05424 (2015). 1505.05424.

37. Fathollahi, A. Machine Learning and Artificial Intelligence Techniques in Smart Grids Stability Analysis: A Review. *Energies* **18**, 3431, DOI: 10.3390/en18133431 (2025). Publisher: Multidisciplinary Digital Publishing Institute.

38. Khlifi, M. K., Boulila, W. & Farah, I. R. Graph-based deep learning techniques for remote sensing applications: Techniques, taxonomy, and applications — A comprehensive review. *Comput. Sci. Rev.* **50**, 100596, DOI: 10.1016/j.cosrev.2023.100596 (2023).

Funding

The authors received no specific funding for this study.

Author contributions statement

B.C. and S.S. conceived the study and B.C. and S.L. developed the methodology. Y.Z. provided software and was responsible for data curation. B.C., S.L. and Y.L. performed validation. B.C. wrote the original draft, and B.C. and S.S. reviewed and edited the manuscript. S.L. prepared the visualization. Y.Z. and Y.L. supervised the project. All authors reviewed the results and approved the final version of the manuscript.

Personal human statement

No personal human data were used in this study.

Competing interests

The authors declare no competing interests.

Additional information

Correspondence and requests for materials should be addressed to Y.Z.